UPCommons

Portal del coneixement obert de la UPC

Aquesta és una còpia de la versió *author's final draft* d'un article publicat a la revista IEEE journal of selected topics in applied earth observations and remote sensing.

URL d'aquest document a UPCommons E-prints:

http://hdl.handle.net/2117/100874

IONOSPHERIC EFFECTS IN GNSS-REFLECTOMETRY FROM SPACE

A. Camps[1,2]*, IEEE Fellow, H. Park*[1,2]*, member IEEE, G. Foti*[3]*, C. Gommenginger*[3]

Email: camps@tsc.upc.edu, hyuk.park@tsc.upc.edu, g.foti@noc.ac.uk, cg1@noc.ac.uk

[1]Department of Signal Theory and Communications, Universitat Politècnica de Catalunya, [2]IEEC/CTE-UPC,
UPC Campus Nord, E-08034 Barcelona, Spain
[3]National Oceanography Centre, Southampton, UK

Abstract

Global Navigation Satellite Systems-Reflectometry (GNSS-R) is an emerging technique that uses navigation opportunistic signals as a multi-static radar. Most GNSS systems operate at L-band, which is affected by the ionosphere. At present, there is only a GNSS-R space-borne scatterometer on board the UK TechDemoSat-1, but in late 2016 NASA will launch the CYGNSS constellation, and in 2019 ESA will carry out the GEROS experiment on board the International Space Station. In GNSS-R, reflected signals are typically processed in open-loop using a short coherent integration time (~1 ms), followed by long incoherent averaging (~1000 times, ~1 s) to increase the signal-to-noise ratio. In this work, the Global Ionospheric Scintillation Model (GISM) is first used to evaluate the total electron content and the scintillation index S4. The ionospheric scintillation impact is then evaluated as a degradation of the signal-to-noise ratio, which can be used to assess the altimetry and scatterometry performance degradation in a generic GNSS-R mission. Since ionospheric scintillations are mostly produced by a layer of electron density irregularities at ~350 km height, underneath most LEO satellites, but closer to them than to the Earth's surface, intensity scintillations occur especially in the GNSS transmitter-to-ground transect, therefore the impact is very similar in conventional and interferometric GNSS-R. Using UK TechDemoSat-1 data, signal-to-noise ratio fluctuations are computed and geo-located, finding that they occur in the open ocean along ~±20° from the geomagnetic equator where S4 exhibits a maximum, and in low wind speed regions, where reflected signals contain a non-negligible coherent component.

Index Terms— GNSS-R, altimetry, scatterometry, ionosphere, scintillations, signal-to-noise ratio

I. INTRODUCTION

The use of Global Positioning System (GPS) signals as signals of opportunity to perform scatterometry was first proposed in 1988 [1], and then in 1993 for mesoscale ocean altimetry [2]. The first evidence that GPS navigation signals could be collected and tracked after being scattered on the sea surface dates back to 1991 when a French aircraft was testing a GPS receiver [3]. With the advent of other satellite navigation systems either global (GNSS) or regional (RNSS) such as Glonas, Galileo, Beidou, IRNSS, and QZSS, or satellite based augmentation systems such as WAAS, EGNOS, MSAS… the number of transmitting satellites is dramatically increasing, thus providing potentially more simultaneous observations. In 1996 it was proposed to use the reflection of the GPS signals from the oceans to extend ionospheric measurements in satellites carrying single frequency radar altimeters [4].

From the originally proposed applications (wind speed and altimetry), many others have been developed including wind speed and direction measurements, ice altimetry, soil moisture, vegetation height and biomass, snow depth.... Also, from the interferometric technique (iGNSS-R) originally proposed [2], several other techniques have been developed: the first GNSS-Reflectometers implemented in the mid 90's used the so-called conventional technique (cGNSS-R) [5], and more recently the reconstructed-code technique (rGNSS-R) has been devised to combine the advantages of both the conventional and the interferometric techniques[1].

The first GPS-R data from space was found in fragments of SIR-C data without radar returns [7]. The first dedicated space-borne GPS-Reflectometer was a secondary payload consisting of a L1 C/A data logger with an 11.8 dB antenna gain, on board the UK-DMC satellite, launched in September 2003 [8], demonstrating the feasibility of GPS reflectometry from ocean, ice and land surfaces. More recently, in July 2014 the UK TDS-1 mission was successfully launched [9] carrying an improved secondary L1 C/A Code GNSS-R payload (SGR-ReSI), with options for

---

[1] In conventional GNSS-Reflectometry (cGNSS-R) the observables are obtained from the cross-correlation of the reflected signal and a locally-generated replica of the transmitted one. In interferometric GNSS-Reflectometry (iGNSS-R) the observables are obtained from the cross-correlation of the reflected and direct signals. In reconstructed-code GNSS-Reflectometry (rGNSS-R), the encripted codes are estimated thanks to the fact that they are transmitted simultaneously at L1 and L2 frequencies. Once the P-code is estimated, the cGNSS-R approach is implemented, which eliminates the need for large multi-beam antennas. The cross-correlation for different delays and Doppler frequencies is called the Delay Doppler Map or DDM, and the cut of the DDM in the delay variable, passing through the DDM peak is called the waveform [6].

Galileo E1, GPS L2C, Glonass L1, GPS L5, Galileo E5, and on-board data processing [10]. At present, three other missions are planned: i) in June 2016 the [3]Cat-2 (pronounced "cubeCat-2") nano-satellite mission will be launched to test the dual-frequency (L1+L2), dual-polarization (right and left hand circular polarizations) PYCARO payload [11], ii) in October 2016 NASA will launch the CYGNSS mission [12], a constellation of 8 microsatellites carrying the same payload as the UK TDS-1 for hurricane monitoring, and iii) in 2019 ESA will carry out the GEROS experiment on board the International Space Station (GEROS-ISS) to perform dual-frequency, polarimetric GNSS-Reflectometry observations for altimetry, scatterometry, and GNSS-Radio Occultations for atmospheric applications [13].

The vast majority of GNSS systems operate at L-band[2] (1-2 GHz). Below 3 GHz, the ionosphere affects the propagation of electromagnetic waves. The main effects are: a rotation of the polarization plane (Faraday rotation), refraction and variation in the direction of arrival, absorption, dispersion, additional propagation delay, and amplitude and phase scintillations [14].

In GNSS systems, circular polarization is used to avoid Faraday rotation, and the polarization mismatch that would occur when trying to receive signals from several satellites simultaneously. For example, at L1 (f_{L1} = 1575.42 MHz), for a 30° elevation path, and a total electron content of 100 TECU (1 TECU = 10^{16}e/m^2) refraction is estimated [14] to be ≤ 14 seconds of arc, the variation in the direction of arrival ≤ 12 seconds of arc, absorption due to polar caps and aurorae[3] ≤ 0.02 dB, dispersion i$\leq$ ~2ns for a chip duration of ~0.1 μs (e.g. GPS P-code), and $\leq$ ~0.2ns for a chip duration of ~1 μs (e.g. GPS C/A-code). At L2 (f_{L2}= 1227.60 MHz) these effects are 1.65 = $(f_{L1}/f_{L2})^2$ times larger than at L1, since they vary with the inverse of the square of the frequency. Dispersion at L2, is even larger than at L1: 2.11 = $(f_{L1}/f_{L2})^3$ times larger, since it varies with the inverse of the third power of the frequency. Despite these values, the above mentioned effects can be neglected at both bands for GNSS-R. Non-negligible effects are explored below.

The ionospheric range error $I(f)$ (expressed in meters) at the frequency f, can be computed as a function of the Slant Total Electron Content ($STEC = \int N_e(\vec{r})d\vec{r}$, where $N_e(\vec{r})$ is the electron density [e$^-$/m^3] along the transect $\vec{r}$:

$$I(f)_{[m]} = \frac{0.403 \cdot STEC_{[TECU]}}{f^2_{[GHz]}}. \qquad (1)$$

The ionospheric range can be quite significant, for example: for $STEC$ = 100 TECU, $I(f_{L1})$ = 16.24 m, and $I(f_{L2})$ = 26.74 m, therefore estimation and compensation techniques are required. However, these errors are negligible in front of the length of the correlation window (i.e. 1500 m in GEROS-ISS), which means that the correlation peak will always lie in the correlation window. Single frequency navigation receivers use worldwide ionospheric models such as the Klobuchar [15] or NeQuick [16] to estimate and compensate the ionospheric range error[4]. Dual-frequency receivers use a linear combination of code ($\rho_{L1,2}\,[m]$) and carrier phase ($\phi_{L1,2}\,[m]$) measurements that compensates up to first order (99.9%) the ionospheric range errors:

$$\Phi_{\text{ionosphere-free}\,[m]} = \frac{f^2_{L1} \cdot \phi_{L1} - f^2_{L2} \cdot \phi_{L2}}{f^2_{L1} - f^2_{L2}}, \qquad (2)$$

$$R_{\text{ionosphere-free}\,[m]} = \frac{f^2_{L1} \cdot \rho_{L1} - f^2_{L2} \cdot \rho_{L2}}{f^2_{L1} - f^2_{L2}}. \qquad (3)$$

On the other hand, localized irregularities in the ionosphere TEC act as convergent and divergent lenses focusing and defocusing electromagnetic waves. These effects are called scintillations and affect the intensity, phase, and angle-of-arrival of the signal. The intensity of the scintillations is characterized by σ_ϕ, the standard deviation of the phase fluctuations, and by the scintillation index (S_4) defined as:

$$S_4 = \sqrt{\frac{\langle I^2 \rangle - \langle I \rangle^2}{\langle I \rangle^2}}, \qquad (4)$$

being I the intensity of the signal.

Figure 1 shows the predicted S_4 index for the Southern Hemisphere autumn equinox (DOY 091) for GPS L1 (1575.42MHz), low magnetic activity and high solar activity (smoothed sunspot number =150) at GPS L1 assuming a) 12:00 h Universal Time, and b) a 23:00 h constant local at all longitudes (from [18]). As it can be appreciated, there are two zones of intense scintillation, one at high latitudes and the other one centered around

---

[2] Except the Indian Regional Navigational Satellite System (IRNSS) that will transmit at L5 (1176.45 MHz) and S band (2492.08 MHz).

[3] Polar cap absorption occurs in periods of high solar activity at geomagnetic latitudes greater than 64°, and lasts on the order of days, while auroral absorption occurs in periods on the order of hours.

[4] "The TEC estimated by the NeQuick model up to 20000 km showed good statistical agreement with the experimental values from the GPS observations (…)" although "there may be a small positive bias to the model estimates" [17]. In addition, the rms of the differences between the observed and modeled STEC variations for 6 representative International GNSS Service (IGS) stations, at different geomagnetic latitudes in both hemispheres, was computed and found not be less than 2 TECU (Fig. 10 of [18]).

±20° of the magnetic equator, where the depth of the scintillation fading ranges from 2 to more than 20 dB depending on the solar activity [14], and it has time constants from 0.5 to 2 s. Low latitude scintillations appear around the sunset (from 19 to 24 h), and around the vernal and autumn equinoxes, and close to the Solar cycle maximum. Scintillation events can last from 30 min to hours. At mid latitudes scintillation occurs exceptionally, e.g. during geo-magnetic storms. Unlike low latitude scintillations, high latitude scintillations depend on space weather events, the geo-magnetic latitude, and can appear at any local time. Phase scintillations have a significant impact on phase-sensitive systems such as space-borne radars (e.g. defocussing SAR images), some ground-based radio-astronomy facilities, and if sufficiently severe, it may stress phase-lock loops in GPS receivers resulting in a loss of phase lock.

In all GNSS-R techniques, the reflected signals are typically processed in open-loop using a model of the geoid to estimate the delay in order to center the tracking window, with short coherent integration times (on the order of 1 ms), followed by long incoherent averaging (~1000-10,000 times: 1-10 s) so as to increase the signal-to-noise ratio (see [6] for a review of the different GNSS-R techniques and applications). Therefore, unlike in GNSS receivers, in GNSS-Reflectometry phase scintillations do not affect the performance of GNSS-R, but amplitude scintillations do.

As it has been seen, in space-borne GNSS-R most ionospheric effects including phase scintillations do not affect the waveform or Delay-Doppler Map shape (basic GNSS-R observables), so that they can be neglected. For altimetry applications the ionospheric range error can be compensated for using dual-frequency receivers. Actually, these observations can be used to generate STEC maps underneath the satellite [4;19]. However, amplitude scintillations produce large fluctuations in the received power ($P_{peak-to-peak} = 27.5 \cdot S_4^{1.26}$ [14]) that will degrade the quality of the GNSS-R observables, both for scatterometry and altimetry applications.

This study is then focused on the impact of intensity scintillations on space-borne GNSS-Reflectometry. It is organized as follows:

- In Section II, the slant electron content (proportional to the ionospheric range error) and the scintillation index S_4 are computed for each transect (transmitter-LEO receiver, transmitter-ground, and ground-LEO receiver) using the Global Ionospheric Scintillation Model (GISM). Intensity fluctuations are characterized as a function of the geographic coordinates, the universal time, and its dependence with the off-nadir angle from where the reflections are picked up, and the sensitivity to the solar flux around some nominal conditions.
- In Section III, taking into account that the time-domain intensity scintillations have a Nakagami pdf with "m-coefficient" $m = 1/S_4^2$, a numerical model is developed to

estimate the impact of the predicted S_4 values on the rms fluctuations of the waveforms' peak (signal-to-noise ratio), both for cGNSS-R and iGNSS-R. Since in both cases, results are very similar, and empirical function is provided to perform quick estimates on the ultimate degradation in the performance of GNSS-R instruments.

- In Section IV, TDS-1 data is analyzed, quality filtered for large antenna gain, and geo-referenced. The standard deviation of the measured SNR is computed and mapped. It is found that in open oceans, these data points correspond to regions around the geomagnetic equator, and low winds.
- Finally, Section V summarizes the main conclusions of this study.

II. IONOSPHERIC RANGE ERRORS AND INTENSITY FLUCTUATIONS FOR LEO GNSS-R INSTRUMENT

The Global Ionospheric Scintillation Model (GISM) model [21] is the model adopted by the ITU-R to predict trans-ionospheric radio propagation. It uses the Multiple Phase Screen technique (MPS), that solves the parabolic equation propagation for a medium dividing it into successive layers, each of them acting as a phase screen. The link between transmitter and receiver can be arbitrary, and it can go through the entire ionosphere or just through a part of it. This is an important feature when studying GNSS-R instruments in Low Earth Orbit (LEO) because, although the ionosphere maximum electron density is ~350 km, where scintillation is generated, it actually extends from ~50 km to more than ~1000 km. Without loss of generality, in the following a LEO GNSS-R receiver located at the International Space Station (ISS) at 400 km height will be assumed.

Figure 2 shows an example of the Vertical (θ=0°) Slant Electron Content[5] (SEC) Electron Content maps in TECU computed using GISM for a Solar Flux[6] equal to 120 SFU, date February 28th, 2015, and Universal Times: 0 h (first column), 6 h (second column), 12 h (third column), and 18 h (fourth column), for the paths: GNSS Space Vehicle (SV)-to-ISS (upper row), GNSS SV-to-ground (middle row), and ground-to-ISS (bottom

---

[5] In this work the term Slant Electron Content (SEC) is used instead of the Slant Total Electron Content (STEC) to emphasize the fact that the transect does not cross the whole ionosphere, but just part of it.

[6] The radio emission from the Sun (F) is measured in Solar Flux Units (1 SFU = 10^{-22} W·m^{-2}·Hz^{-1}) at 10.7 cm wavelength, and correlates with the Sunspot number (R): F = 67.0 + 0.572 R + $(0.0575$ R$)^2$ - $(0.0209$ R$)^3$. Solar flux varies typically from ~50 SFU to ~275 SFU.

row). As it can be appreciated, a wave of increased electron density[7] moves West-wards along the geomagnetic equator with increasing universal time, because ionosphere electrons are created by the radiation coming from the Sun. In addition, about 40% of the TEC is below the LEO receiver, while the other 60% is above it. These figures show that the ionospheric range error (I, Eqn. 1) corresponding to the GNSS Space Vehicle (SV)-to-ISS transect cannot be neglected. Since I is proportional to the electron content, as for ground GNSS receivers, it can also be almost completely compensated for using dual-frequency observations for the up- and down-looking observables, or it can be partly compensated using models [15, 16].

Figure 3 shows the computed SEC maps in [TECU] at Universal Time = 6 AM (left panels), and the corresponding Scintillation Index S_4 maps (right panels) for the three paths: a) Transmitting GNSS SV-to-ISS, b) Transmitting GNSS SV-to-ground, and c) Transmitting ground-to-ISS (bottom row). The upper row corresponds to a GNSS SV located at the zenith, that is a GNSS reflection at an incidence angle $\theta_i=0°$. The middle row: shows the average SEC computed for a reflection at $\theta_i = 35°$ coming from the North, West, South and East directions. Finally, the last row shows the standard deviation computed from these four directions, to show if a single value can be used for each incidence angle, or if a different value must be used in each direction.

As expected, the computed values of SEC are larger than those at nadir by ~$\sec(\theta_i)$. However, SEC variations as large as 1-3 TECU can be expected depending on the azimuth direction. This means an ionospheric range error of 1-3 TECU = 16-49 cm at L1 and 27-80 cm at L2, which –if not corrected for using dual-frequency receivers and using ionosphere-free observables (Eqn. (3))- represents a large fraction of the altimetry expected performance of PARIS IoD [22] or the GEROS-ISS requirements [23] ($\sigma_h \leq 30$ cm$_{rms}$). For single frequency GNSS-R altimeters it may be very difficult to achieve meaningful mesoscale altimetry observations, although with coarse resolution.

When studying the variation of the scintillation index S_4 for each transect it becomes apparent that the intensity scintillations occur in the SV-to-ground path, because the layer of electron density irregularities (or "phase screen") is at 350 km height, far away from the ground surface.

Intensity also exhibits non-negligible azimuthal variations as well. In the other two transects $S_4=0$, and in particular in the ground-to-ISS the distance of the layer of electron density irregularities (or "phase screen") to the ISS is small. This means that both conventional and interferometric GNSS-R types of instruments will be affected in a similar way by intensity scintillations.

Figure 4 is similar to Fig. 3, but it shows the incremental values of SEC (ΔSEC in [TECU]) and S_4 (ΔS_4 [no units]) when the solar flux is increased from 120 to 130 SFU. As it can be appreciated, waves of S_4 follow those of SEC (Fig. 3), but delayed in local time. The change in the SEC can be larger than 6 TECU for the SV-to-ground transect, and 3-4 TECU for the SV-to-ISS transect, corresponding to 6 TECU = 98 cm at L1 and 160 cm at L2. Again, despite these values are 3-5 times larger than the expected altimetry performance of PARIS IoD [22] or the GEROS-ISS requirements [23], they can be corrected for using dual-frequency receivers to compute ionosphere-free observables (Eqn. (3)), but cannot be corrected for with the models used in ground GNSS receivers [15, 16].

Finally, Fig. 5 shows the difference in the computed S_4 index at f_5 (L5/E5) and f_1 (L1/E1). As it can be appreciated, the S_4 index is up to 0.2 units larger for the SV-to-GND transect, and up to 0.01-0.02 larger very specific regions of the SV-to-ISS transect. This means that: i) the lower frequency bands will suffer more from intensity fluctuations than the higher frequency bands, although intensity fading is in both bands is correlated because it is originated by the same irregularities in the ionosphere, and that ii) interferometric GNSS-R may suffer in some particular locations from a slightly decrease of the performance due to the intensity scintillation in the direct signal path. This last point will be numerically quantified in the next Section.

III. IMPACT OF INTENSITY FLUCTUATIONS ON THE GNSS-R OBSERVABLES

The statistics of the instantaneous variation of intensity of the received signal is adequately described given by a Nakagami density function:

$$p(I) = \frac{m^m}{\Gamma(m)} \cdot I^{m-1} \cdot e^{-m \cdot I}, \qquad (5)$$

where $m = 1/S_4^2$, and the intensity I is normalized to one.
In order to assess the impact of the ionospheric scintillation in the different transects SV-to-ISS, SV-to-ground, and ground-to-ISS, the computed S_4 values have been used to generate a three different time-series of intensity fluctuations using the Cornell Scintillation Model [24]. Figure 6

---

[7] Note: for this particular simulation GISM predicted a peak of ~60 TECU in the TX-> GND transect, while UPC TEC maps indicate that VTEC values are around 90 to 100 TECU for the same date. GISM has been used for consistency with the parametric analysis performed below.

shows simulated intensity and phase time series at L1/E1 and L5/E5 computed for $S_4=0.7$ (strong scintillation) at $f_{L1/E1}$ and a correlation time $\tau_0=0.5$ s. Note the deep intensity fadings due to ionospheric scintillation, and the cycle slips when such deep fadings occur. Note also that the effects are more pronounced at L5/E5 than at L1/E1.

At this time, for cGNSS-R the time series of the intensity fluctuations are computed as the product of the intensity fluctuations of the SV-to-ground ($I_{SV-GND}(t)$) and ground-to-ISS (reflected signal only: $I_{GND-ISS}(t)$), and for iGNSS-R as the product of the intensity fluctuations of the three transects: SV-to-ground ($I_{SV-GND}(t)$) and ground-to-ISS (corresponding to the reflected signal: $I_{GND-ISS}(t)$), and SV-to-ISS (corresponding to the direct signal: $I_{SV-ISS}(t)$). The Noise-to-Signal Ratio (NSR) is then computed as the ratio of the standard deviation of the intensity fluctuations (variance of the signal intensity fluctuations), and the mean intensity.

$$NSR_{cGNSS-R} = \frac{\sigma_{I_{SV-GND}(t) \cdot I_{GND-ISS}(t)}}{\langle I_{SV-GND}(t) \cdot I_{GND-ISS}(t) \rangle}, \quad (6a)$$

$$NSR_{iGNSS-R} = \frac{\sigma_{I_{SV-GND}(t) \cdot I_{GND-ISS}(t) \cdot I_{SV-ISS}(t)}}{\langle I_{SV-GND}(t) \cdot I_{GND-ISS}(t) \cdot I_{SV-ISS}(t) \rangle}, \quad (6b)$$

In the absence of ionospheric scintillations ($S_4 = 0$) the intensity is constant, and the NSR = 0 (linear units). In the presence of ionospheric scintillations ($S_4 > 0$), NSR > 0. The process is repeated 20 times and the estimated NSR are averaged.

Figure 7 shows the computed Noise-to-Signal Ratio increase (ΔNSR) maps due to ionospheric amplitude scintillation index S_4 for a) conventional GNSS-R and b) interferometric GNSS-R, for 1) transmitting GNSS SV at zenith, and 2) average of ΔNSR values for transmitting GNSS SV producing a reflection at $\theta_i = 35°$ coming from the North, West, South and East directions. (to be added to the NSR computed including the received signal powers, instrumental errors, and speckle noise).

As expected, the largest impact occurs where S_4 is the largest, along the geo-magnetic equator, and it is very similar for both cGNSS-R and iGNSS-R, since most of the intensity scintillations occur in the SV-to-ground transect, which is common to both techniques, and very little scintillations occur in the direct signal transect. Finally, Fig. 8 shows the numerically computed ΔNSR in linear units, as a function of the scintillation parameter S_4 for both cGNSS-R and iGNSS-R, which are nearly the same. An excellent polynomial fit is given in Eqn. (7):

$$\Delta NSR = 0.71 \cdot S_4^3 - 0.6 \cdot S_4^2 + 0.88 \cdot S_4. \quad (7)$$

which can be used to make quick estimations of the ionospheric scintillation impact on cGNSS-R

and iGNSS-R for scatterometry and altimetry [22] applications.

In this particular example (date and solar flux = 120 SFU), the ΔNSR reaches a value of ~0.4. Since ionospheric scintillations are uncorrelated from other error sources, the impact on the final SNR can be estimated as:

$$\frac{1}{SNR} = \frac{1}{SNR_{no \; scintillation}} + \Delta NSR. \quad (8)$$

This means that for typical SNR values[8] over ice, ocean, and land: 2.8 dB (1.9 lin), 4.4 dB (2.75 lin), and -1.9 dB (0.65 lin), the ionospheric scintillations degrade the SNR down to 0.34 dB (1.1 lin), 1.2 dB (1.3 lin), and -2.9 dB (0.5 lin), respectively.

IV. SEARCHING IONOSPHERIC SCINTILLATION SIGNATURES IN TDS-1 DATA

Ionospheric Scintillation Signatures are searched in a data set from TDS-1 spanning from September 1st, 2014 to February 5th, 2015. Data are quality filtered first for large antenna gain (larger than 12 dB), and geo-referenced. A glimpse of the 1 s data (DDMs computed with 1 ms coherent integration time and 1000 incoherent averages) is presented in Figs. 9 and 10. Figure 9a shows the uncalibrated signal power [dBAU][9] computed as the average power over a 1.5 KHz x 1 chip window centered around the peak position of the Delay-Doppler Map. The dynamic range is ~20 dB, and the highest peaks are found over iced regions in the Northern and Southern hemispheres, possibly due to a specular reflections, and in some continental regions where an exaggerated increase of the noise power (Fig. 9b) is also present, most likely due to radio-frequency interference or jammers. The uncalibrated noise power [dBAU] is computed as the average power over a 10 KHz x 1 chip window in the signal-free area of the DDM, before the leading edge of the waveform. Figure 9c shows the Signal-to-Noise Ratio (SNR) in [dB] computed as the difference in [dB] between the uncalibrated signal power [dBAU] and the uncalibrated noise power [dBAU]. The highest SNRs are found again in the iced regions (80° N and 70° N), North America and North Europe, Plata river mouth in South America, and some scattered regions in Asia and the Sahara desert. It is worth noting that there are two "bands" in the ocean regions around ±20° latitude, with some scattered spots of high SNR. Figure 9d shows the standard deviation in [dB] of the SNR time series,

5

computed in a sliding window of 21 consecutive samples.

In order to gain more insight on the nature of these "bands", Fig. 10a shows the geo-referenced map of ASCAT A/B 10 m height wind speed collocated with TDS-1 GNSS-R data (1h/1deg) [m/s], and Fig. 10b the standard deviation of the measured signal-to-noise ratio [dB] (as Fig. 9d) coincident with ASCAT A/B 10 m height wind speed data. By comparing Fig. 10b with Fig. 1b, it becomes more apparent now that, except for a few points close to the coast, where the standard deviation is higher because of the land-sea transition, the points of larger standard deviation follow the geo-magnetic equator (e.g. North of Australia, Atlantic coast of Argentina, and similarly around +20°N, although there are not that many data points over the ocean).

Finally, Fig. 11 shows the scatter plot of collocated ASCAT A/B 10 m height wind speed (Fig. 10a) vs. TDS-1 SNR [dB] (Fig. 9c): a) for all antenna gains, b) for an antenna gain larger than 12 dB, and c) for an antenna gain larger than 12 dB and SNR standard deviation less than 0.5 dB. As it can be appreciated, most of the data points exhibiting a standard deviation larger than 0.5 dB correspond to wind speeds smaller than ~4-5 m/s (there are some around ~7 m/s, and just one at ~14 m/s). The interpretation for these results is the following: if the wind speed is low, the reflection is almost specular, coming from a narrow region over the ocean surface (the first Fresnel zone, on the order of ~500 m and 6.5 km[10]) and there is a strong coherent component, which can then be affected by the ionospheric scintillations. If the wind speed is moderate or high, the reflection becomes diffuse (incoherent), coming from a much larger region over the ocean surface (the so called "glistening zone", of tenths of kilometers), and therefore it is not affected by ionospheric scintillation, because scintillation is basically a phenomenon related to the coherence of the electromagnetic waves. Ionospheric scintillation effects add to the complexity of interpreting GNSS-R signals at low wind speed, which have been shown to respond also to other geophysical conditions such as sea state [25].

V. CONCLUSIONS

The impact of the ionosphere in GNSS-R instruments in LEO has been studied. Due to the way the data is processed (short coherent integration time, followed by long incoherent averaging), only ionospheric range errors and intensity scintillations are important.

The Global Ionospheric Scintillation Model (GISM) has been used to compute maps of the slant electron content (SEC) in the three following transects: transmitting space vehicle-to-ground,

transmitting space vehicle-to-LEO receiver, and ground-to-LEO receiver. Since the SEC values are different, ionospheric range errors cannot be corrected for using the Klobuchar or NeQuick models developed for ground receivers, and their correction requires dual-frequency receivers to form ionosphere-free observables for each transect.

Intensity scintillation is analyzed for the three different transects as well, and parameterized in terms of the S_4 parameter. Since the region where scintillation is produced is at ~350 km height, lower than most LEO heights, it is found that scintillation mostly occurs in the transmitting space vehicle-to-ground, therefore it affects in a very similar way both the conventional and the interferometric GNSS-R techniques. The degradation of the SNR has been numerically evaluated by computing realistic time series of ionospheric intensity scintillations (Cornell Scintillation Model), and computing the Noise-to-Signal Ratio (NSR) increase. A polynomial fit has been obtained to relate in a simple way the NSR and S_4. This formulation can be easily used to predict the degradation of the performance of upcoming generic GNSS-R instruments in LEO orbit, both for altimetry and scatterometry applications, or to perform an instrument trade-off study, i.e. the performances of TDS-1 with an antenna directivity of ~13 dB, cannot be the same as those of the upcoming GEROS experiment on board the International Space Station with an antenna directivity of ~22-24 dB.

Finally, TDS-1 data has been analyzed and the standard deviation of the measured SNR has been computed, mapped, and compared to the collocated ASCAT A/B wind speed. It is found that in open oceans, these data points correspond to regions around ±20° from the geomagnetic equator, and low winds, which is an indirect experimental evidence that a coherent scattered component exists, since it is the only one that can suffer from intensity scintillation. At wind speeds higher than ~5-7 m/s the scattering of the electromagnetic waves is mostly incoherent, coming from very large regions (much larger than the size of the ionosphere irregularities), and intensity scintillations do not take place.

References
[1] Hall, C.D., and R.A. Cordey, "Multistatic Scatterometry," in Geoscience and Remote Sensing Symposium, 1988. IGARSS '88. Remote Sensing: Moving Toward the 21st Century, International , vol.1, no., pp.561-562, 12-16 Sept. 1988
[2] Martín-Neira, M., "A PAssive Reflectometry and Interferometry System (PARIS): Application to ocean altimetry", ESA J., vol. 17, no. 4, pp. 331-355, 1993.

---

[10] The 6.5 km elongation is basically due to the satellite ground track speed and the incoherent averaging.

[3] Auber, J. C., A. Bibaut, and J. M. Rigal, "Characterization of multipath on land and sea at GPS frequencies", Proceedings of the 7th International Technical Meeting of the Satellite Division of the Institute of Navigation, pp. 1155-1171, 1994.

[4] Katzberg, S. J., & Garrison, J. L. (1996). Utilizing GPS to determine Ionospheric delay over the ocean. NASA Technical Memorandum 4750.
http://ntrs.nasa.gov/archive/nasa/casi.ntrs.nasa.gov/19970005019.pdf

[5] Garrison, J. L., and S. J. Katzberg, "Detection of ocean reflected GPS signals: Theory and experiment", Proceedings of 1997 IEEE Southeastcon, Blacksburg, USA, April 1997.

[6] Zavorotny, V. U., S. Gleason, E. Cardellach, and A. Camps, "Tutorial on Remote Sensing Using GNSS Bistatic Radar of Opportunity," in Geoscience and Remote Sensing Magazine, IEEE , vol.2, no.4, pp.8-45, Dec. 2014

[7] Lowe, S.T.; J. L. LaBrecque, C. Zuffada, L. J. Romans, L. E. Young, and G. A. Hajj, "First spaceborne observation of an Earth-reflected GPS signal," Radio.   Sci., 37(1), doi:10.1029/2000RS002539, 2002.

[8] Gleason, S., S. Hodgart, Y. Sun, C. Gommenginger, S. Mackin, M. Adjrad, and M. Unwin, "Detection and Processing of bistatically reflected GPS signals from low Earth orbit for the purpose of ocean remote sensing," in Geoscience and Remote Sensing, IEEE Transactions on , vol. 43, no. 6, pp. 1229-1241, June 2005

[9] M. Unwin, P. Jales, J. Tye, C. Gommenginger, G. Foti, J. Rosello, "Spaceborne GNSS-Reflectometry on TechDemoSat-1: Early Mission Operations and Exploitation," IEEE Journal of Selected Topics in Applied Earth Observations and Remote Sensing, Vol. 9, No. 10, October 2016, doi:10.1109/JSTARS.2016.2603846

[10] The SGR-ReSI Space GNSS Instrument:
http://www.sstl.co.uk/Products/Subsystems/Navigation/SGR-ReSI (last visited, November 17th, 2015)

[11] Carreno-Luengo, H., A. Camps, R. Jove-Casulleras, A. Alonso-Arroyo, R. Olive, A. Amezaga, D. Vidal, and J.F. Munoz, "The 3Cat-2 Project: GNSS-R In-Orbit Demonstrator for Earth Observation," Proceedings of the 4S Symposium, Small Satellites systems and Services, 26-30 May 2014, Porto Petro, Mallorca, Spain. Available on line: http://congrexprojects.com/2014-events/4S2014/proceedings   (last visited November 17th, 2015).

[12] Ruf, C. S., S. Gleason, Z. Jelenak, S. Katzberg, A. Ridley, R. Rose, J. Scherrer, and V. Zavorotny, "The CYGNSS nanosatellite constellation hurricane mission", Proceedings of the 2012 IEEE International Geoscience and Remote Sensing Symposium, pp. 214-216, Munich, Germany, July 2012.

[13] J. Wickert, E. Cardellach, M. Martín-Neira, J. Bandeiras, L. Bertino, O. Andersen, A. Camps, N. Catarino, B. Chapron, F. Fabra, N. Floury, G. Foti, C. Gommenginger, J. Hatton, P. Hoeg, A. Jäggi, M. Kern, T. Lee, Z. Li, H. Park, N. Pierdicca, G. Ressler, A. Rius, J. Roselló, J. Saynisch, F. Soulat, C.K. Shum, M. Semmling, A. Sousa, J. Xie, and C. Zuffada, "GEROS-ISS: GNSS REflectometry, Radio Occultation and Scatterometry onboard the International Space Station," submitted to IEEE Journal of Selected Topics in Applied Earth Observations and Remote Sensing, 2016.

[14] Ionospheric propagation data and prediction methods required for the design of satellite services and systems, Recommendation ITU-R P.531-6.   Available   on   line: https://www.itu.int/dms_pubrec/itu-r/rec/p/R-REC-P.531-6-200102-S!!PDF-E.pdf (last visited: November 17th, 2015).

[15] Klobuchar, J., "Ionospheric Time-Delay Algorithms for Single-Frequency GPS Users," IEEE Transactions on Aerospace and Electronic Systems (3), pp. 325-331, 1987

[16] Di Giovanni, G. and Radicella, S. M., "An analytical model of the electron density profile in the ionosphere," Advances in Space Research. 10(11), pp. 27-30, 1990.

[17] Kersley, L., D. Malan, S. Eleri Pryse, L.R. Cander, R.A. Bamford, A. Belehaki, R. Leitinger, S.M. Radicella, C. N. Mitchell, and P. S.J. Spencer, "Total electron content – A key parameter in propagation: measurement and use in ionospheric imaging," Annals of Geophysics, supplement to vol. 47, n. 2/3, pp. 1067- 1091, 2004

[18] Hernandez-Pajares, M., "Performance of IGS Ionosphere TEC Maps," IGS Ionosphere Working Group, Date: 03/04/2003, Issue: 1.0 Rev: 2

[19] Pallares, J. M.; G. Ruffini and L. Ruffini, "Ionospheric tomography using GNSS reflections," in IEEE Transactions on Geoscience and Remote Sensing, vol. 43, no. 2, pp. 321-326, Feb. 2005.

[20]   About   Ionospheric   Scintillation: http://www.sws.bom.gov.au/Satellite/6/3   (last visited November 17th, 2015)

[21] Trans-ionospheric radio propagation: The Global Ionospheric Scintillation Model (GISM): http://www.itu.int/pub/R-REP-P.2097-2007   (last visited November 15th, 2015).

[22] Camps, A.; Park, H.; Valencia i Domènech, E.; Pascual, D.; Martin, F.; Rius, A.; Ribo, S.; Benito, J.; Andrés-Beivide, A.; Saameno, P.; Staton, G.; Martín-Neira, M.; D'Addio, S.; Willemsen, P.; "Optimization and Performance Analysis of Interferometric GNSS-R Altimeters: Application to the PARIS IoD Mission," in IEEE Journal of Selected Topics in Applied Earth Observations and Remote Sensing, vol. 7, no. 5, pp. 1436-1451, May 2014.

[23] GNSS Reflectometry, Radio Occultation and Scatterometry onboard ISS (GEROS-ISS): SYSTEM REQUIREMENTS DOCUMENT, Reference TEC-ETP/2013.202/MMN, Issue 2, Revision 3, Date of Issue: 08/06/2015

[24] Humphreys, T. E., M.L. Psiaki, J.C. Hinks, B. O'Hanlon, and P.M. Kintner, "Simulating Ionosphere-Induced Scintillation for Testing GPS

Receiver Phase Tracking Loops," in Selected Topics in Signal Processing, IEEE Journal of , vol.3, no.4, pp.707-715, Aug. 2009

[25] Foti, G., C. P. Gommenginger, P. Jales, M. Unwin, A. G. P. Shaw, Y. C. Robertson, and J. Rosello, "Preliminary Analyses and Validation of New Spaceborne GNSS-Reflectometry Data from the UK TechDemoSat-1 Mission for Ocean Wind Retrieval," in IEEE International Geoscience and Remote Sensing Symposium 2015 (IGARSS), 26-31 July 2015, Milan, Italy.

ALL FIGURES (EXCEPT FIGURE 8) TO BE PLACED IN 2 COLUMNS.

a) b)
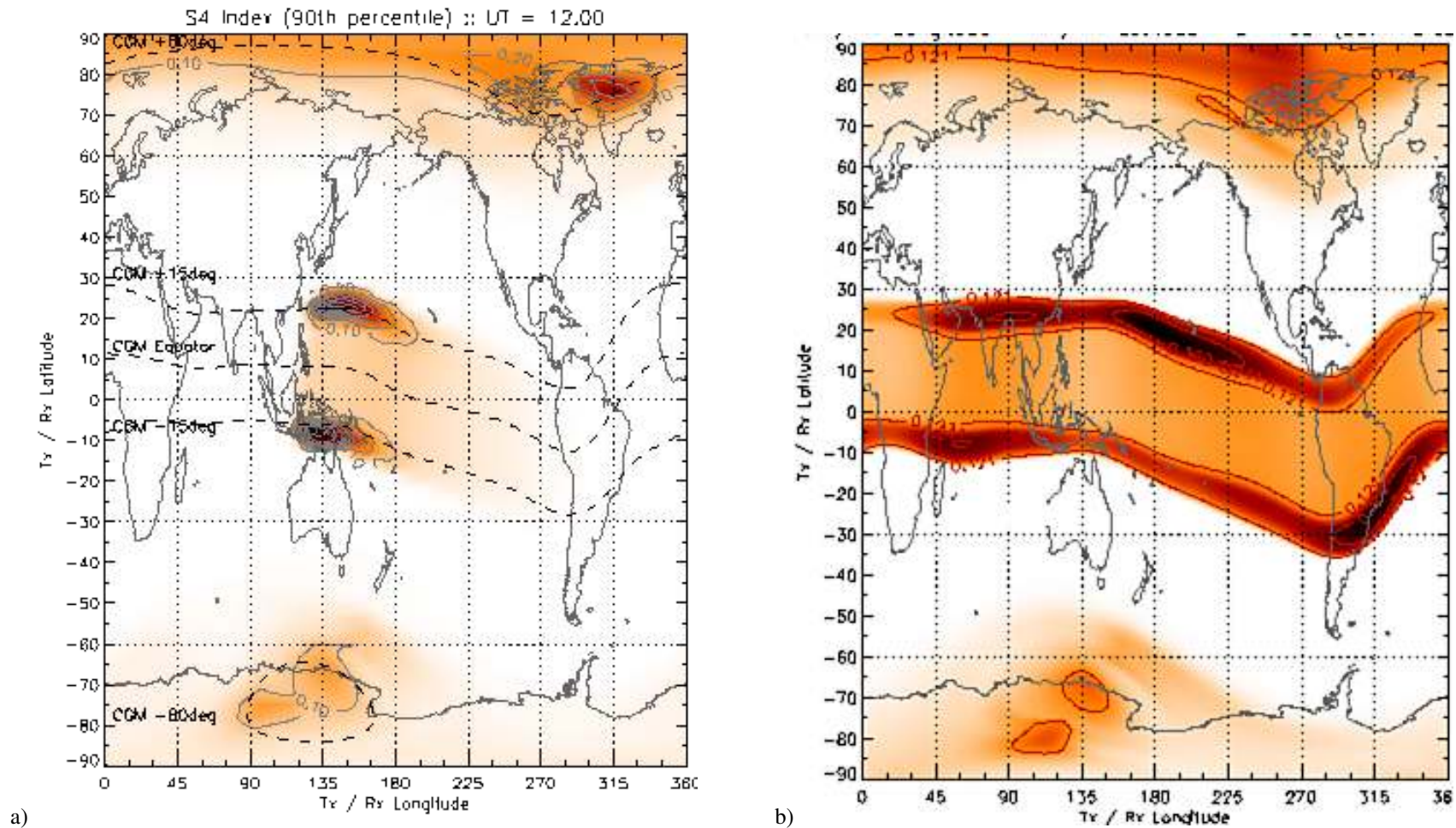
Fig. 1. a) Predicted S_4 index at the Southern Hemisphere autumn equinox (DOY 091) for GPS L1, low magnetic activity and high solar activity (smoothed sunspot number =150) assuming Universal time (12:00 h). Dashed lines represent lines of constant geomagnetic latitude, b) S_4 Scintillation index at GPS L1 assuming constant local time (23:00 h) at all longitudes (from [19]).
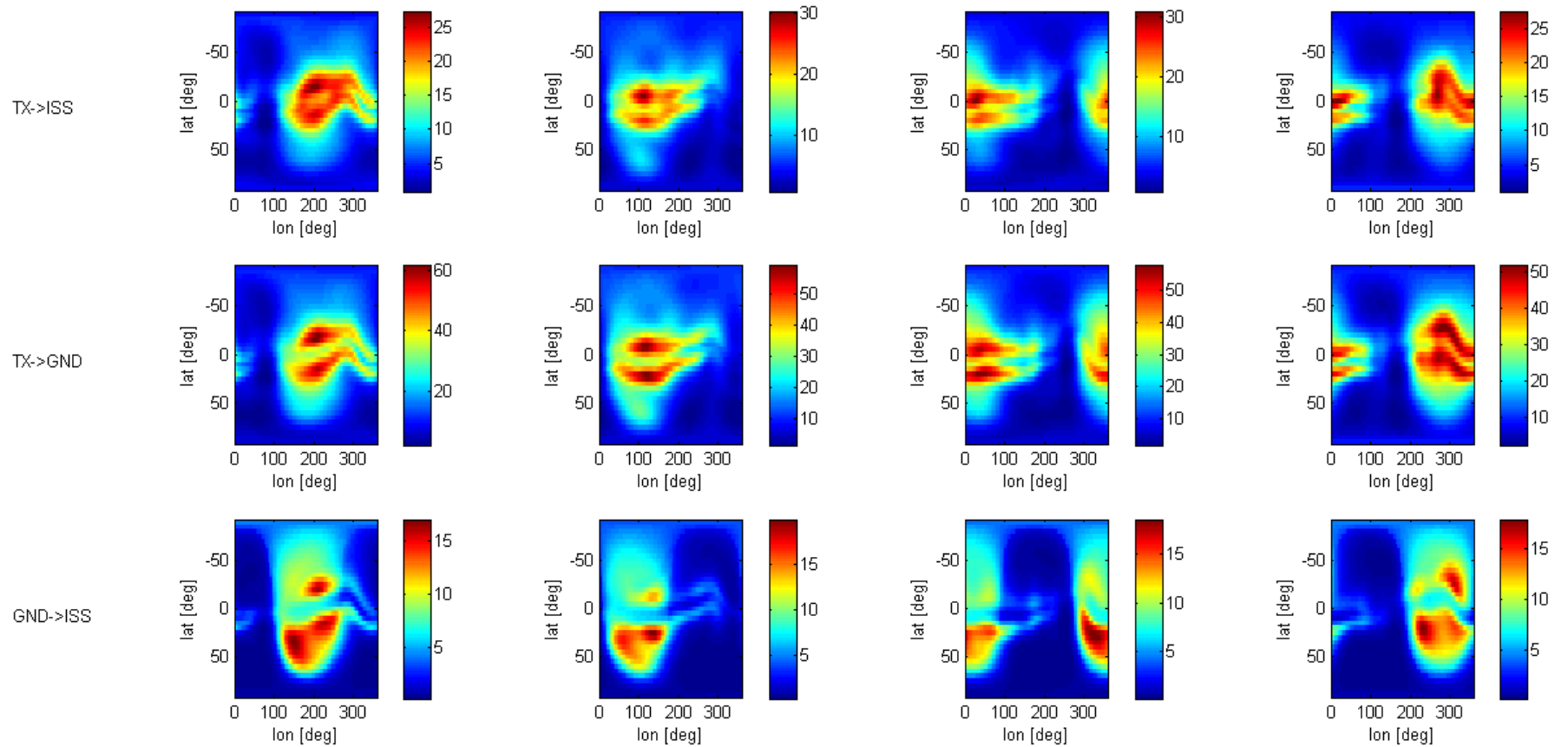
Fig. 2. Slant (θ=0°) Electron Content maps in [TECU] for a Solar Flux equal to 120 SFU, date February 28th, 2015, and Universal Times: 0 h (first column), 6 h (second column), 12 h (third column), and 18 h (fourth column), for the paths: GNSS SV-to-ISS (upper row), GNSS SV-to-ground (middle row), and ground-to-ISS (bottom row).
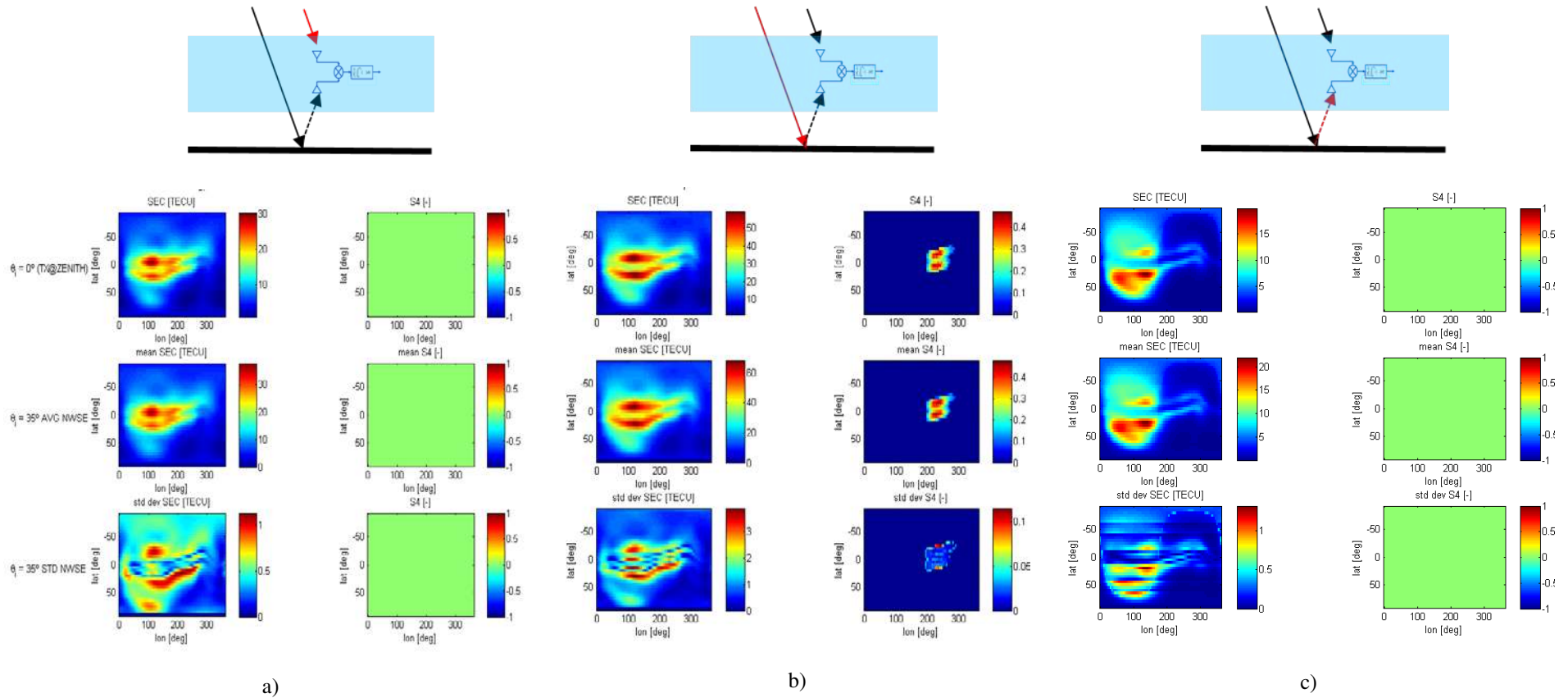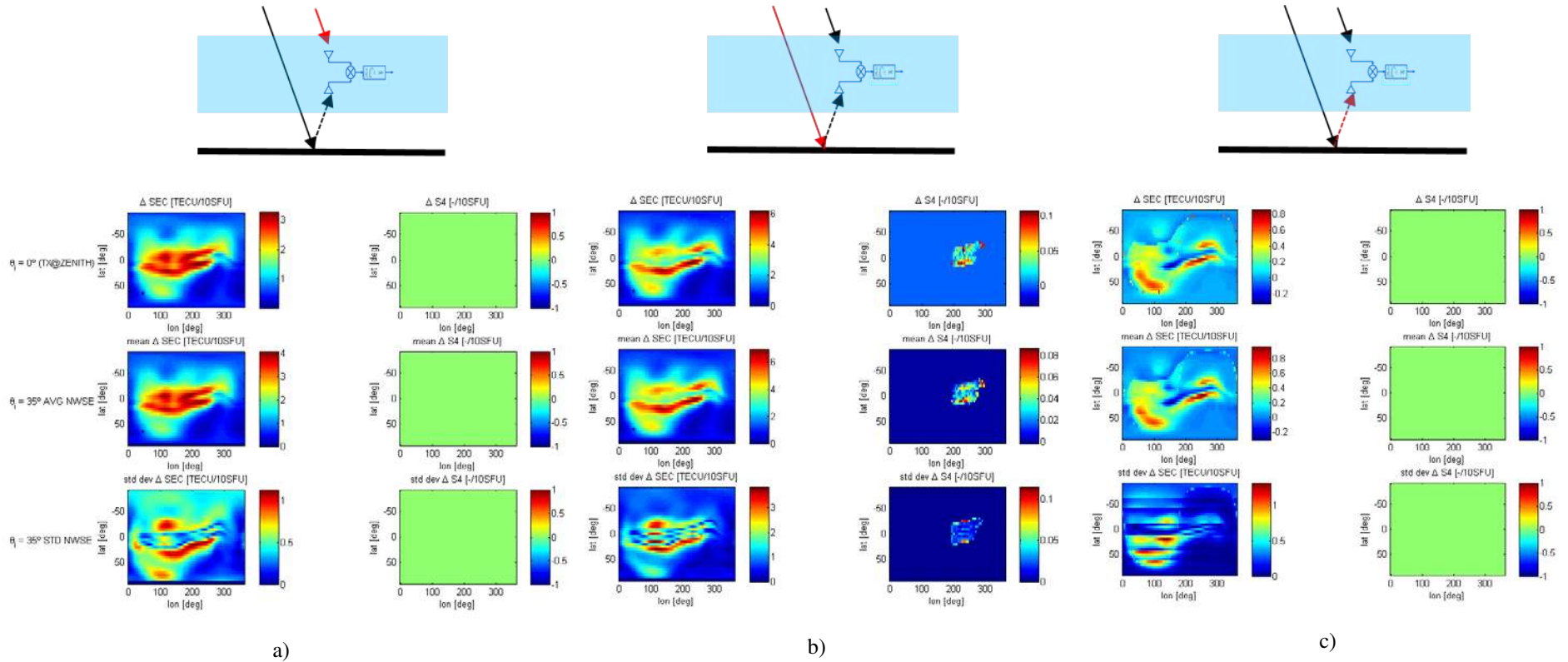
Fig. 3. Slant Electron Content maps in [TECU] at Universal Time = 6 AM (left panels), and corresponding Scintillation Index S4 maps (right panels) for paths: a) Transmitting GNSS SV-to-ISS, b) Transmitting GNSS SV-to-ground, and c) Transmitting ground-to-ISS (bottom row). Upper row: SEC for GNSS SV at zenith, middle row: average SEC for a reflection at $\theta_i = 35°$ coming from the North, West, South and East directions, and bottom row: standard deviation of the SEC computed for a reflection at $\theta_i = 35°$ coming from the North, West, South and East directions.

Fig. 4. Slant Electron Content increment maps in [TECU] at Universal Time = 6:00 h (left panels), and corresponding incremental Scintillation Index S4 maps (right panels) when solar activity increases from 120 SFU to 130 SFU, for paths: a) Transmitting GNSS SV-to-ISS, b) Transmitting GNSS SV-to-ground, and c) Transmitting ground-to-ISS (bottom row). Upper row: SEC for GNSS SV at zenith, middle row: average SEC for a reflection at θ_i = 35°coming from the North, West, South and East directions, and bottom row: standard deviation of the SEC computed for a reflection at θ_i = 35°coming from the North, West, South and East directions.
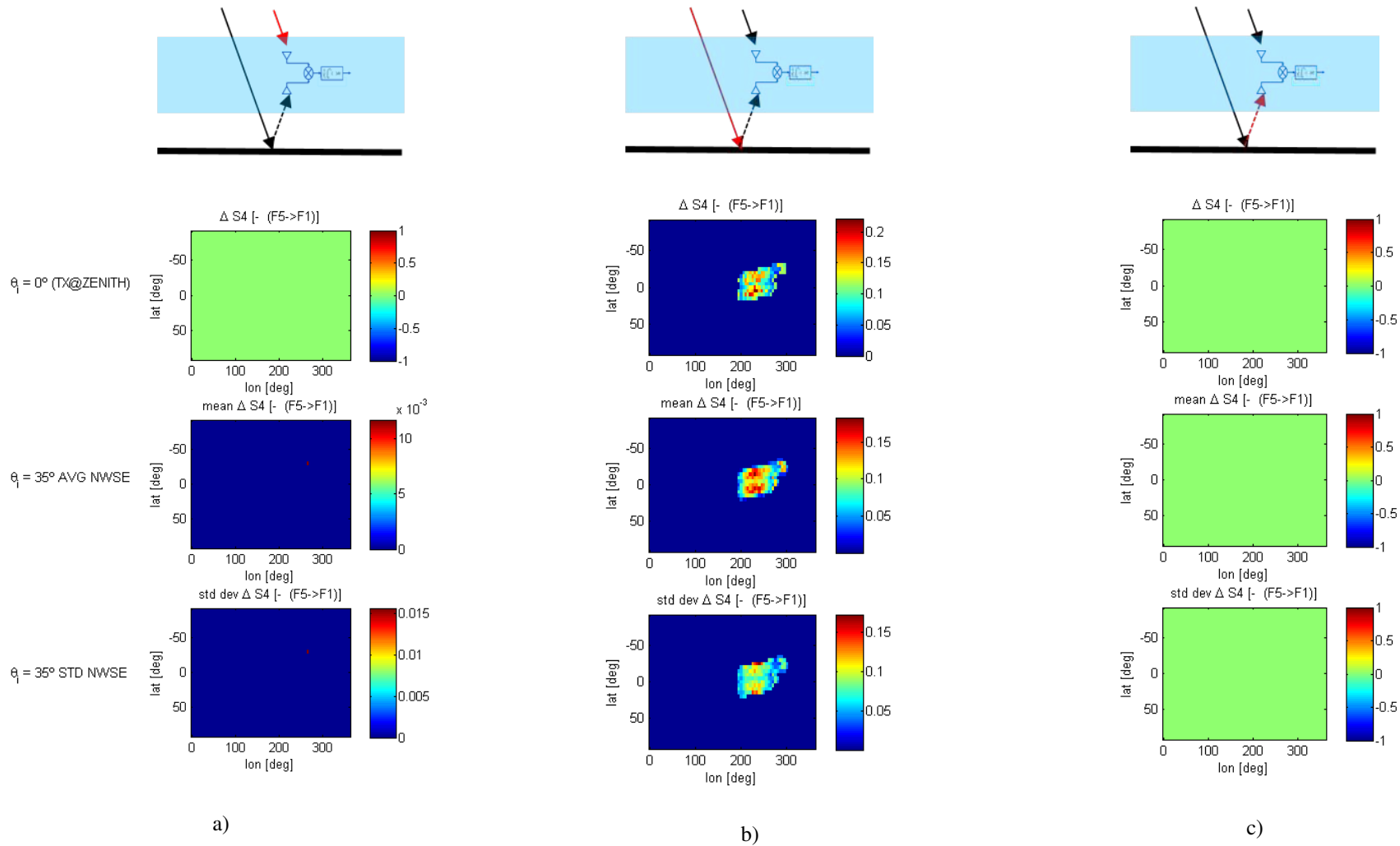
Fig. 5. Differential Scintillation Index S_4 maps (at L5/E5 minus L1/E1) for Universal Time = 6:00 h and solar activity = 120 SFU, for paths: a) Transmitting GNSS SV-to-ISS, b) Transmitting GNSS SV-to-ground, and c) Transmitting ground-to-ISS (bottom row). Upper row: SEC for GNSS SV at zenith, middle row: average SEC for a reflection at $\theta_i = 35°$ coming from the North, West, South and East directions, and bottom row: standard deviation of the SEC computed for a reflection at $\theta_i = 35°$ coming from the North, West, South and East directions.
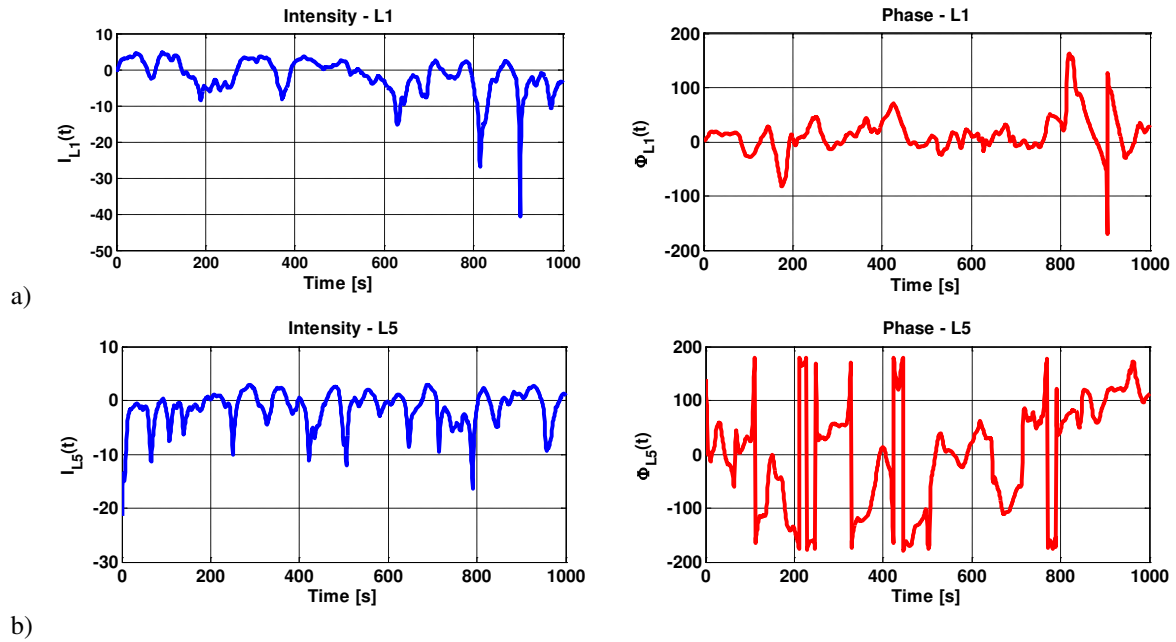
Fig. 6. Simulated intensity and phase time series at a) L1/E1 and b) L5/E5 computed for S_4=0.7 at $f_{L1/E1}$, and a correlation time τ_0=0.5 s. Note the cycle slips when deep fadings occur.
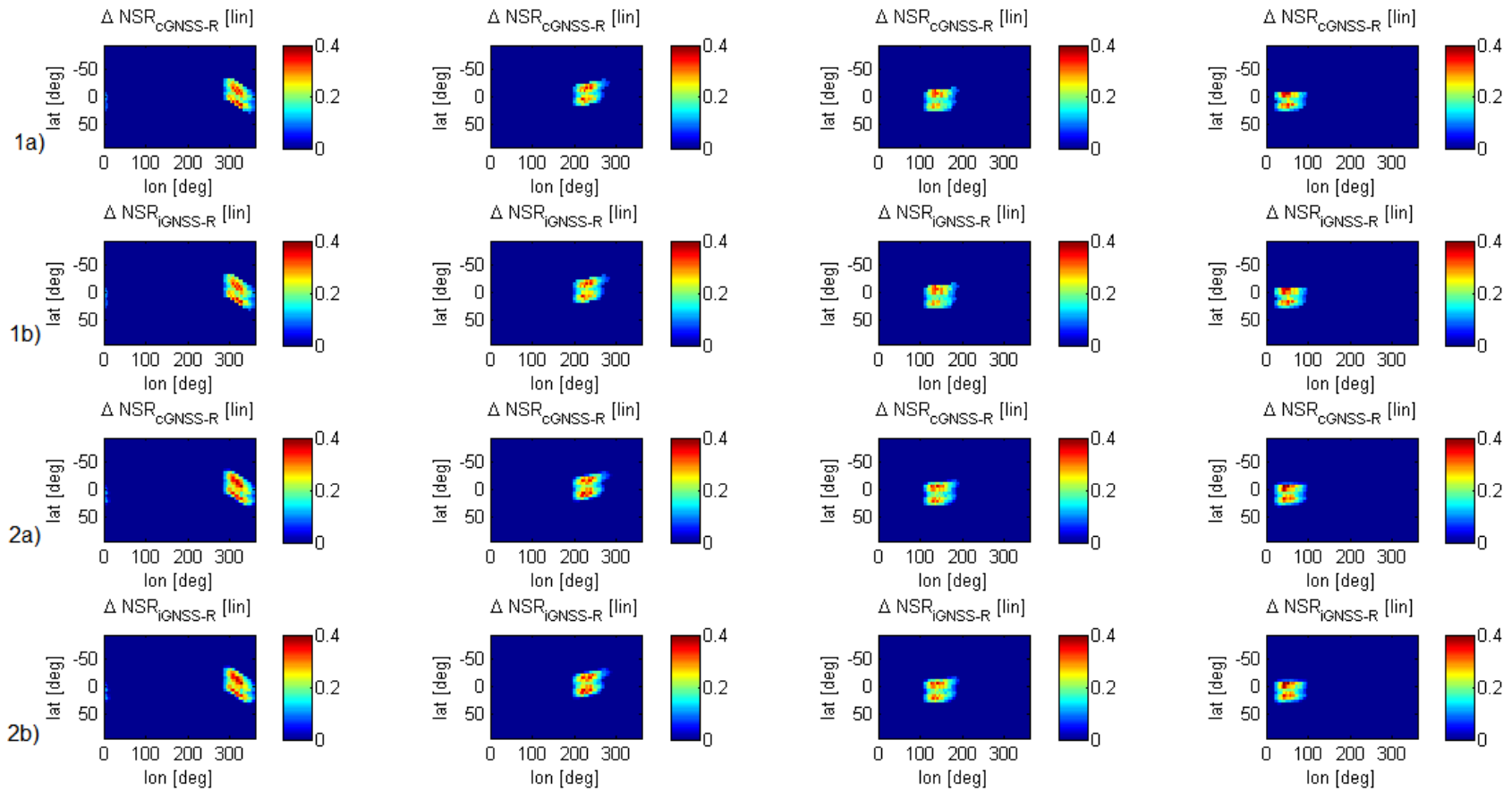
Fig. 7. Noise-to-Signal Ratio (NSR) increase at L1 (other conditions as in previous plots) due to ionospheric amplitude scintillation index S4 for a) conventional GNSS-R and b) interferometric GNSS-R, for 1) transmitting GNSS SV at zenith, and 2) average of ΔNSR values for transmitting GNSS SV producing a reflection at $\theta_I = 35°$ coming from the North, West, South and East directions
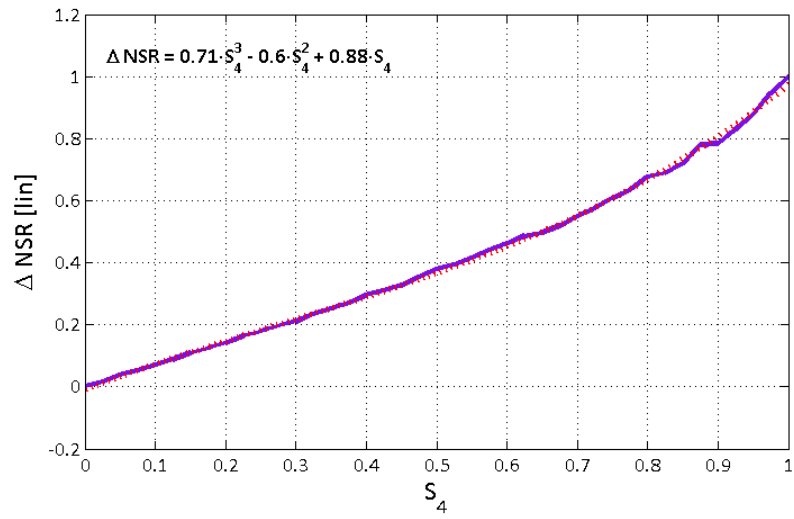
$$\Delta NSR = 0.71 \cdot S_4^3 - 0.6 \cdot S_4^2 + 0.88 \cdot S_4$$

Fig. 8. Increase of the Noise-to-Signal Ratio (linear units) as a function of the scintillation parameter S_4. Solid line: numerically simulated ΔNSR, dotted line: polynomial fit.
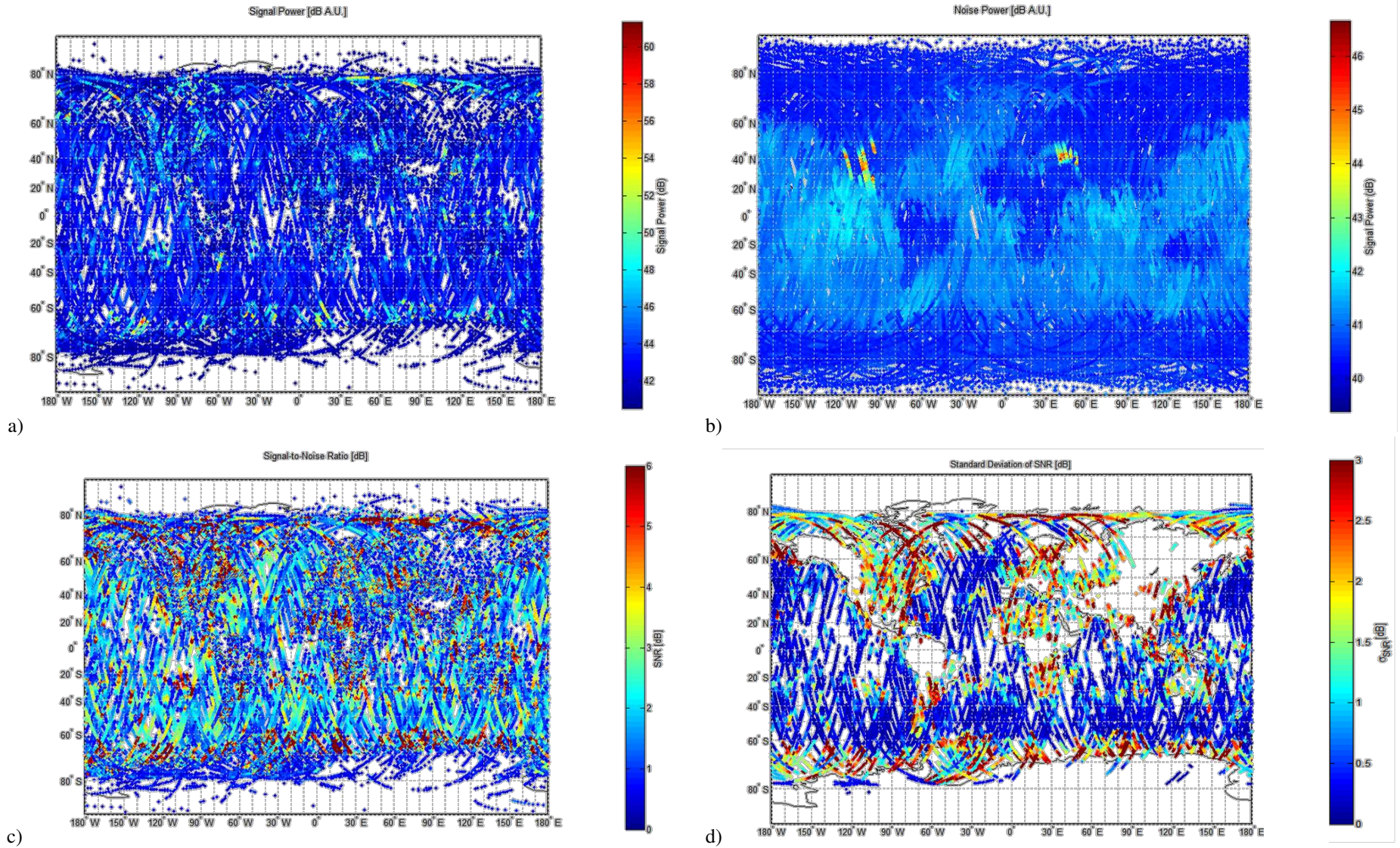
Fig. 9. Geo-referenced maps of: a) Uncalibrated TDS-1 GNSS-R signal power [dBau], b) uncalibrated TDS-1 GNSS-R noise power [dBau], c) signal-to-noise ratio [dB] (scale truncated to 6 dB), d) standard deviation of the measured signal-to-noise ratio [dB] computed from a sliding window of 21 consecutive data.
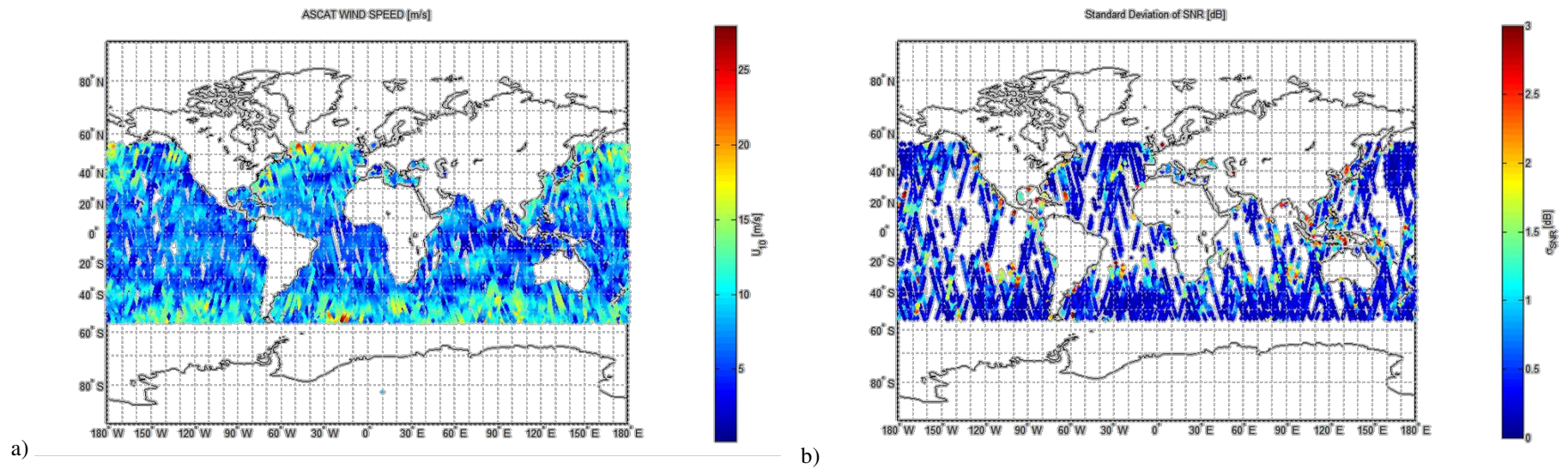
Fig 10. Geo-referenced maps of: a) ASCAT A/B U_{10} collocated with TDS-1 GNSS-R data (1h/1deg) [m/s], and b) Standard deviation of the measured signal-to-noise ratio [dB] (as Fig. 9d) coincident with ASCAT A/B U_{10} data.
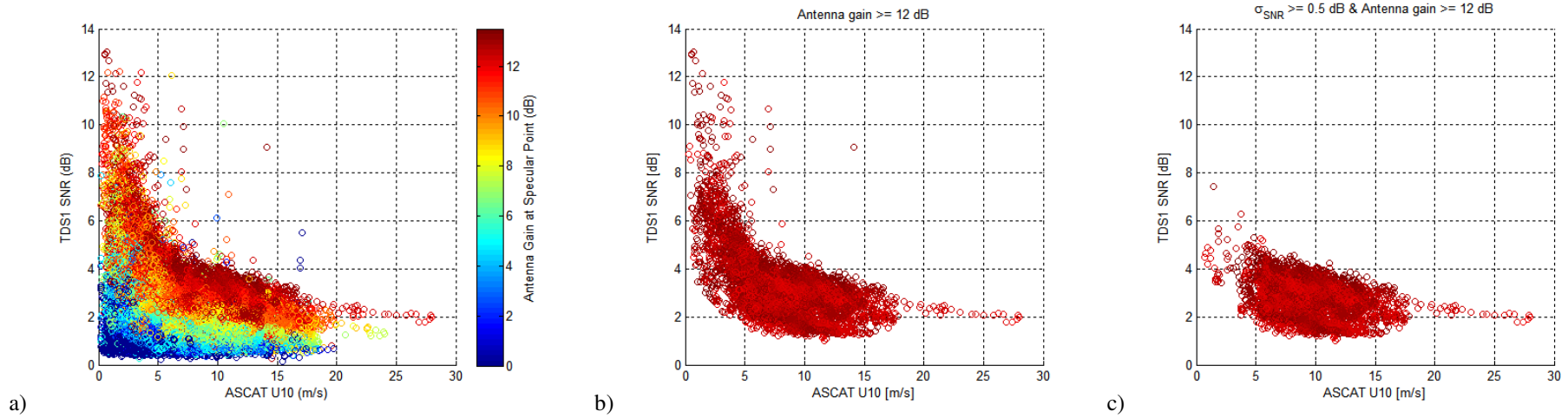
Fig 11. a) Scatter plot of TDS-1 SNR data vs. ASCAT A/B U_{10}. Colorscale indicates the antenna gain. b) Same as a), but only for antenna gain larger than 12 dB. c) Same as b) but only data points with SNR standard deviation smaller than 0.5 dB.